Impacts of soil moisture content on simulated mesoscale circulations during the summer over eastern Spain

(Atmospheric Research, 2015, 164-165: 9-26. DOI: 10.1016/j.atmosres.2015.04.015: http://www.sciencedirect.com/science/article/pii/S0169809515001301)

I. GÓMEZ[a], V. CASELLES[a,b], M. J. ESTRELA[b,c]

[a] *Departament de Física de la Terra i Termodinàmica, Facultat de Física, Universitat de València, Doctor Moliner, 50, 46100 Burjassot, Valencia, Spain.*

[b] *Laboratorio de Meteorología y Climatología, Unidad Mixta CEAM-UVEG, Charles R. Darwin, 14, 46980 Paterna, Valencia, Spain.*

[c] *Departament de Geografia, Facultat de Geografia i Història, Universitat de València, Avda. Blasco Ibáñez, 28, 46010 Valencia, Spain.*

Correspondence to: Vicente Caselles

E-mail: Vicente.Caselles@uv.es

ABSTRACT

The Regional Atmospheric Modeling System (RAMS) version 6.0 has been used to investigate the impact and influence of initial soil moisture distributions on mesoscale circulations. To do this, two different events have been selected from the 2011 summer season: one at the beginning of the season (June) and the other one at the end of the season (August). For each of these mesoscale frameworks a total of five distinct simulations were performed varying the initial soil moisture content: a control run and four additional sensitivity tests. The control run, corresponding to a low soil moisture content, is the one used within the real-time weather forecasting system implemented in the Valencia Region. In the corresponding sensitivity simulations this low value has been progressively increased in different steps until the original soil moisture content doubled. It has been found that high soil moisture is associated with colder near-surface temperature, a moister relative humidity and a slightly lower near-surface wind speed, whereas a drier soil resulted in a dryer relative humidity, warmer temperature and a slight low-level wind. In general, the highest soil moisture contents are required to reproduce the near-surface daily cycles of temperature and relative humidity through higher values of latent heat flux and lower values of sensible heat flux. In this regard, moistening the soil improves the previous results obtained using the RAMS configuration used within the operational forecasting system. However, the wind speed is not quite sensitive to changes in the soil moisture content over flatter terrain. Finally, although a warming and dryer mixing layer is obtained with the lowest soil moisture content, the mixing layer height remains practically unchanged when using the distinct configurations over flat terrain. These differences are enhanced over more complex terrain.

Keywords: RAMS model, soil moisture, boundary layer, mesoscale modelling, numerical weather prediction/forecasting.

1. Introduction

Mesoscale circulations are a characteristic atmospheric phenomenon in many coastal areas, and this has been amply documented. Nevertheless, the study of this mechanism is still interesting due to its importance to human affairs as well as its role in air pollution transport and precipitation (Miao et al., 2003). These circulations prevail in contrast to other meteorological conditions during the summer months over Eastern Spain (Azorin-Molina et al., 2009; Azorin-Molina et al., 2011; Miró et al., 2009). Increased solar heating in the surrounding mountains results in convective mixing and the onset of upslope winds, aside from this the wind reverses and drainage flows are established during the evening or night. Thus, a typical daily cycle is recognized based on combined local and regional forcings (Millán et al., 2000).

An operational forecasting system (OFS) based on the latest version of the RAMS model (Pielke et al., 2013) (Version 6.0) and covering a large extension of the Western Mediterranean coast was running operationally for the summer 2011 (Gómez et al., 2014, Gómez et al., 2015) as a support to different alert and warning systems (Gómez et al., 2010). Considering the RAMS simulations performed by this tool, rather accurate results have been found. However, some differences have still been detected in terms of meteorological surface variables, such as temperature, humidity and wind speed (Gómez et al., 2014, Gómez et al., 2015). Although the model reproduces the diurnal variation in relative humidity properly, it has been observed that the model shows more difficulties in forecasting this magnitude at night time. In addition, in terms of temperature, there is a general tendency to over-predict the observations both at night and day time, notably marked by the latter. In this case, the Bias score of 0.3 ºC obtained at night time rises to 3 ºC during the day. Finally, the wind speed is

overestimated, with the greatest differences found at day time, when the wind flow is more complex (considering that wind speeds are much higher than during the night).

Bearing in mind that mesoscale circulations are of most significant importance in the study area and the differences found in terms of the meteorological surface variables provided by the OFS, the current paper is focused on the understanding of the impact of the volumetric soil moisture content (SM hereafter) on these kinds of meteorological episodes and their forecast accuracy.

The impacts of different land surface characteristics on sea-breeze dynamics is well documented (Kala et al., 2010). For example, Physick (1980) found that the inland penetrations of the sea breeze vary significantly with SM. In addition, higher evapotranspiration from a wetter soil implies more energy in the form of latent heat and less in sensible heat, and hence, a reduction in the intensity of the sea breeze. These results have been confirmed by several sea-breeze modelling studies (e.g., Yan and Anthes 1988; Miao et al. 2003). Similarly, Ma and Lyons (2000) varied SM in their simulations of the western sea breeze in the south-west of Western Australia and found wetter soils delayed sea-breeze onset. Miao et al. (2003) investigated the effects of SM, topography, and land degradation caused by the sea breeze over Eastern Spain, covering the area of the current study. Miao et al. (2003) also used RAMS (Version 3b), by conducting simulations with current (heterogeneous) land cover and measured SM, as well as homogeneous forest, short grass, and desert land cover with 60, 25, and 10% SM respectively. They found that lower SM resulted in higher horizontal and vertical wind components at all heights as well as a more penetrative sea breeze. Another recent study used an increasing SM of 0.25 m^3m^{-3} in relation to their control simulation, using the RAMS model focused on a sea breeze event in the South-West of Western Australia (Kala et al., 2010).

On the other hand, different approaches have been used to evaluate the influence of SM on numerical simulated results, but applied to other kinds of meteorological episodes. In this regard, Quintanar et al. (2008), using the Penn State/NCAR's Mesoscale Model (MM5), and Suarez et al. (2014), using both MM5 and RAMS performed similar studies over Western Kentucky (USA). The focus of these latest two investigations was to examine three synoptic events with varying synoptic force occurring on June, 2006. Several simulations were conducted in which initial SM was increased and decreased by 0.05, 0.10 and 0.15 m^3m^{-3}. Three-member wet and dry ensembles were constructed and analysed with respect to control (CTRL hereafter) runs for each study period in order to evaluate the response of the PBL to changes in SM. Finally, Husain et al. (2014) used the GEM (Global Environmental Multiscale) model in order to investigate the influence of SM on surface-layer atmosphere. In this case, different simulations from the control run were performed with varying initial values of SM. The sensitivity analysis were based on increasing or reducing by 33% the SM level in order to make the signals attributable to its changes on near-surface meteorology more apparent.

Accordingly, the aim of our study is to investigate the possible impacts of SM variations by using the latest version of the RAMS model (Pielke et al. 2013) (Version 6.0). Here, the intention is double. On the one hand, the primary objective of the current paper is to assess the influence in RAMS responses to modified initial SM conditions under mesoscale circulations. Contrary to the previously mentioned studies, we start with a RAMS control run that corresponds to the SM homogeneous initialization used within the OFS. In this case, a low value of 0.20 m^3m^{-3} was used to perform the RAMS operational simulations. Then we progressively increased this initial volumetric SM by 50%, 75%, 90% and 100% with respect to the CTRL run, as explained in detail in the

next section. On the other hand, the second objective of this paper is to compare the RAMS forecasts with surface and upper air observations so as to determine whether there is a SM value able to reproduce the measurements with a better accuracy with the aim of improving the OFS original results. To do this, we have focused on two selected events from the 2011 summer season: 25-26 June and 11-12 August. The idea was to choose one event at the beginning of the season and another one during the same season, to test whether differences on mesoscale circulations arise within the summer. In addition, the former was selected corresponding to a situation where clear skies dominated the atmospheric conditions and the latter was selected as a situation with cloudiness prone to precipitation and summer storms inland (Teruel Province, Fig. 1; Azorin-Molina et al., 2014).

The paper is organised as follows: Section 2 contains a description of the study area as well as the model configuration and the observational datasets used. In addition, a detailed description of the experimental design is also provided in this section. In section 3, we introduce the synoptic framework for the simulated periods and the model results. Finally, section 4 is devoted to the concluding remarks.

2. Site characterisation, model aspects and methodology.

The area of study is located on the East coast of the Iberian Peninsula. This region is bordered by the Mediterranean Sea in its Eastern part and surrounded by high mountain ranges, exceeding 1,500 m height, near the coast (Fig. 1). Solar heating in this area frequently creates thermally induced mesoscale circulations that develop under clear sky conditions, with strong diurnal variations, and with patterns and intensities that depend on the regional surface energy budget and orography (Pérez-Landa et al., 2007). In order to clarify the discussion of results, several identifiers have been included in Fig. 1.

As it has been pointed out, the atmospheric model used in this study is the RAMS model (Cotton et al., 2003; Pielke, 2013), in its version 6.0. The model's domain consists of three nested domains (Fig. 1). The coarser domain (D1) covers the Southern part of Europe at a 48-km horizontal grid resolution and the Mediterranean. The purpose of the domain is to simulate the synoptic features that influence the region of study. The first nested domain (D2) covers the Iberian Peninsula and the Western Mediterranean with a grid resolution of 12 km. Finally, a finer domain (D3) includes an area of Eastern Spain and its adjacent sea with a horizontal grid spacing of 3 km. In addition, 45 levels were selected in the vertical following a stretched scheme, with a 30-m spacing near the surface increasing gradually up to 1,000 m near the top of the model at about 16,000 m and with 15 levels in the lower 1,000 m. Due to the staggered coordinate system, the lowest model vertical coordinate was located at about 15 m AGL.

RAMS was initialised with the Kuo-modified parameterization of sub-grid scale convection processes applied to the coarse domain (Molinari et al., 1985), whereas grids 2 and 3 utilized explicit convection only. Besides, the Mellor and Yamada (1982) scheme is used, as representation of the PBL and surface layer turbulence, along with a full-column, two-stream, single-band radiation scheme that accounts for clouds to calculate short-wave and long-wave radiation (Chen and Cotton, 1983). The cloud and precipitation microphysics scheme from Walko et al. (1995), was applied in all the domains. Finally, RAMS 6.0 was coupled with the Land Ecosystem-Atmosphere Feedback model (LEAF-3), so as to account for the heat and moisture exchange between the soil, vegetation, canopy, surface water and atmosphere; see Walko et al. (2000) for detailed model descriptions.

RAMS was initialized with the National Centre for Environmental Prediction (NCEP) Global Final Analysis (FNL) at 6 h intervals and 1 x 1 degree resolution

globally. In addition, a Four-Dimensional Data Assimilation (FDDA) technique was applied to define the forces at the lateral boundaries of the outermost five grid cells of the largest domain.

As said in the previous section, two different mesoscale frameworks were selected: 25-26 June and 11-12 August 2011. Both atmospheric situations were characterized by the development of the Iberian Thermal Low (ITL; Millán et al., 1997; Millán et al., 2000). For the first period, clear conditions were established over Eastern Spain. For the second period, fair weather was observed on the 11 August as well. Still, a significant cloudiness was detected on the 12 August inland (Teruel Province: Fig. 1) in the morning. This environment developed throughout the day, reaching pre-coastal and coastal areas in the afternoon, leading to precipitation storms in Teruel and Castellón (Fig. 1). Southern areas, such as Alicante, Valencia and Murcia, showed, in general, a cloudless situation, and remained under the influence of mesoscale circulations, even though clouds spread over this area in the late afternoon.

For each of the selected periods, SM was progressively increased until the control (CTRL) simulation SM doubled, using 11 soil levels with higher resolution on the uppermost layers down to a depth 50 cm below the surface for the soil model. The surface energy budget is represented by LEAF-3, which partitions the net radiation into sensible, latent (evaporation plus transpiration), and soil heat fluxes. This scheme includes prognostic equations for SM and soil temperature for multiple layers which are specified by explicit levels in the RAMS initialization. As a result, soil and snow are divided into multiple vertical levels, and vegetation and canopy air are represented by a single level (Walko et al., 2000). The modification of the SM parameter for the sensitivity experiments consists of progressively increasing the initial volumetric SM by 50%, 75%, 90% and 100%, taking the following values: 0.20 (SM20, and corresponding

to the CTRL run), 0.30 (SM30), 0.35 (SM35), 0.38 (SM38) and 0.40 (SM40) m^3m^{-3}. These SM values are homogeneously applied for the whole simulation domain in the model initialization. Thus, a total of five simulations were carried out for both periods. Each simulation was performed for 60 h, with a temporal resolution of 1 h, starting at 12 UTC 24 June 2011 to 25-26 June for the atmospheric situation and at 12 UTC 10 August 2011 to 11-12 August 2011 for the framework. The first 12 h were treated as a spin-up period to avoid possible problems related to this initialization. Consequently, the analysis was performed using the remaining 48 h.

In terms of observational datasets, the Spanish Ministry of Agriculture, Food and Environment operates an automatic surface weather station network through the SIAR (Sistema de Información Agroclimática para el Regadío; Agroclimatic Information System for Irrigation) system. Data from 5 automatic meteorological stations from this network were used to compare with RAMS (Fig. 1). Hourly measures of near-surface temperature, relative humidity, wind speed and direction, and incoming solar radiation from the SIAR stations are available. Likewise, vertical profiles for these meteorological variables corresponding to the 00Z and 12Z Murcia (MUR; Fig. 1) soundings are included and compared with the model. Finally, the down-welling surface short-wave radiation flux (DSSF), obtained by means of the SEVIRI sensor is used to perform a spatial comparison for the RAMS-simulated incoming solar radiation. The method used to retrieve this magnitude for the DSSF product is based on the framework of the OSI SAF (Brisson et al., 1999). This model is designed to compute the effective atmospheric transmittance, applying a clear or cloudy sky retrieval method depending on cloud cover. This latter parameter is provided by the cloud mask developed by the present existing and very short-range forecasting, which is integrated in the LSA SAF operational system (Geiger et al., 2008; LSA SAF, 2015).

3. Results and Discussion

3.1. Comparison between model and measurements

All model runs reveal a general over-estimation of the incoming solar radiation, when lower than 50 W/m^2 (Fig. 2). However, for the 26 June 2011 more differences were observed between SM40 and the other RAMS configurations (Fig. 2c,e,g), where the former under-estimates the observations as well as the results produced by the other cases of initial SM distributions. These deviations have their influence on the temperature field (Fig. 3c,e,g), with an under-estimation of the maximum temperature compared to the one obtained for the other days of simulation. On the other hand, both SM38 and SM40 were forecasting clouds the 12 August toward the coast (Fig. 4d,e). In this case, although the observations show a small cloudiness (Fig. 4f), it is not captured by the lowest SM values contents (Fig. 2b; Fig. 4a,b,c). SM40 simulates clouds over a wider extension than the other initial SM configurations (Fig. 2d; Fig. 4). In this regard, considering the spatial distribution of the incident surface flux of shortwave radiation, Fig. 4d shows that SM38 reproduces the observations better (Fig. 4f) when compared to the SM40 simulation (Fig. 4e).

SM content directly influences the evolution of surface-layer meteorological variables, particularly in the daytime temperature (Husain et al., 2014), as shown in Fig. 3. As expected, increasing the initial SM reduces the daytime 2-m temperature, whereas decreasing the initial SM has the opposite effect in all stations. Although there is not a unique initial SM that better fits all stations, it is observed that, in general, a high SM value is required in order to reproduce the observations. In this sense, Fig. 3 shows that SM38 and SM40 are the simulations with a better performance for the two selected periods. However, in some cases, such as XAT station (Fig. 3e), low SM values show the best performance while forecasting the daytime temperature. Additionally, it is

observed that RAMS does not reproduce significant differences when using the lowest SM values. In this regard, SM30 offers rather similar results to SM20. In the same way, SM35 shows similarities with SM30. However, a slight variation in SM when considering high values of this magnitude (SM38 and SM40), produces more differences in the model results than when using a larger variation, when considering lower values of this parameter (SM20, SM30 and SM35). Finally, although significant differences are obtained at daytime, the deviation among the distinct simulations is considerably reduced at night time. As a result, varying the SM content has a significant impact on daytime temperature, whereas the night time one remains practically unchanged in general.

In terms of relative humidity (Fig. 5), higher values of initial SM reproduce the daily evolution of this magnitude in a better way, although with more difficulties than in the case of temperature. This result is obtained for both periods of simulation. In addition, not only do SM38 and SM40 better capture the night time relative humidity but they also reproduce the daytime value rather more accurately. In this regard, Fig. 5 shows that the significant difference reproduced by the model in relation to the observations during the night within the SM20 simulation is notably reduced using the highest values of SM. On the contrary, some stations still show a visible underestimation for the SM40 run. However, in these cases, it is observed that a bias of about 40% obtained using the SM20 simulation are reduced to differences below 20% having used the SM40 for the June period (Fig. 5a,c), and even lower for the August one (Fig. 5b,d). For inland stations within more complex terrain (Fig. 5i,j), although increasing the initial SM content has a positive impact on the simulated relative humidity at night time, higher values of SM produce an over-estimation of this field during the day, which isn't observed when using lower values of SM, such as the SM20

and the SM30 simulations, where the model remains closer to the observations. Finally, using these low SM contents, we observe a general trend for the moisture field to decrease as the simulation progresses.

The evolution of the 10-m wind speed is presented in Fig. 6. During night time, this magnitude is practically unaffected by any modification in the initial SM content, with the exception of more complex terrain (Fig. 6i,j). However, more differences are observed during the day when considering SM40 in relation to the other SM contents. In this regard, RAMS simulations are more windy when dryer SM values are used in the model initialization. Nevertheless, the effect of moistening the soil has no a significant impact on the 10-m wind speed for stations over coastal and pre-coastal terrain where the orography is not as complex as inland. In the former case, the observations offer values between 2 and 3 m/s, while the model shows values higher than 5 m/s, thus overestimating this meteorological magnitude. In the latter case, although the model still simulates 10-m wind speed around this last value, the observations are as high as 5 m/s as well. As a result, for inland stations, the model reproduces the observations properly, following the diurnal variation observed (Fig. 6g,h,i,j).

Fig. 7 shows that RAMS generally captures the diurnal cycle of the simulated periods quite well, characterized by the daytime development of the sea-breeze advecting air from sea to land, followed by night time surface draining winds oriented from land to sea (Pérez-Landa et al., 2007), and considering the different RAMS simulations. In addition, the u-component is well captured by RAMS generally. However, some differences are found in terms of the wind components over coastal and pre-coastal locations. Considering the SAN and SEG stations, even though the trend of the v-component is properly reproduced by RAMS, this magnitude is overestimated at daytime. In this regard, Fig. 7a-d shows a deviation of the simulated daytime v-

component to the North compared to the observations. In contrast, the model presents more difficulties while forecasting the observed wind direction for XAT station. In this case, the observations show a northerly wind while RAMS simulates a well established easterly wind flow over this area. Besides, Fig. 7 shows that similar results are obtained for the two simulated periods in all cases. Contrasting this figure with Fig. 6, the model behaviour for inland and coastal stations is exposed in terms of the 10-m wind speed.

Different vertical profiles for the MUR sounding (Fig. 1), as predicted by the model for the different SM runs, are shown in Fig. 8 and Fig. 9 for the June and August periods, respectively. Once again, and similar to the near-surface results, the wind direction shows rather small differences between the model and the observations aloft. Fig. 8g,h and Fig. 9g,h show that not only does RAMS capture the near-surface wind direction very well, but also the observed values aloft. In general, RAMS shows a tendency to overestimate the wind speed within the lower troposphere with the opposite trend in upper levels. This result is obtained for all SM contents. During the day, Fig. 8e and Fig. 9f expose that the highest differences within the lower troposphere are obtained using the SM20 simulation. However, at night the opposite trend is observed. Additionally, the night time wind speed for 11 August 2011 is captured very well by RAMS using the different SM runs (Fig. 9e).

SM40 simulates a colder (Fig. 8a,b and Fig. 9a,b) and moister (Fig. 8c,d and Fig. 9c,d) planetary boundary layer (PBL) than the other SM runs both at night and daytime. However, the largest differences, about 3K, are obtained during the day, they are then reduced at night, but with the same trend observed during the daytime. In general, the model shows a tendency to underestimate the mixing layer height compared to the observations. In both periods of simulation, the observed mixing layer height is located at about 1,000 m or higher, while the model locates this layer at about 800-900 m.

Finally, contrasting the distinct SM simulations for the location of the mixing layer height, Fig. 8 and Fig. 9 displays that this layer remains practically unchanged when drying or moistening the soil, slightly enhanced with the lower SM values. Thus, higher initial SM contents do not have a significant impact on the location of the mixing layer height over flatter terrain. Still, as we will see in the next section, differences in SM have a notable impact over more complex terrain.

3.2. Evaluation of simulated PBL parameters

With the aim of evaluating the sensitivity of RAMS-forecasts PBL parameters to varying conditions of SM, this section focuses attention on several variables directly related to the boundary layer processes. This analysis includes the latent and sensible heat fluxes, the long-wave upward radiation and the evaluation of the mixing layer height. Although the availability of measurements of these magnitudes would be truly valuable in order to investigate the accuracy of the model in forecasting different physical processes, no information on these parameters is available over this area of study. However, its comparison of the different SM simulations is still extremely useful as it obtains a deeper understanding of the differences obtained in other available variables, such as those presented in the previous section. This is true considering that PBL parameters affect near-surface magnitudes such as temperature, relative humidity and the wind field. In this regard, it is well known that increased values of available SM result in enhanced evapotranspiration and greater use of daytime radiative energy for latent heat flux that eventually reduces sensible heat flux from the surface to the atmosphere (Husain et al., 2014). As a result, wet soil is generally linked to lower daytime heating of the near-surface atmosphere through release of sensible heat from the surface, and by extension to a lower daytime maximum temperature, as it has already been seen before. As also mentioned in the previous section, the main

differences of the SM modification are obtained during the day, while very low differences are observed at night time.

Thus, we will focus on analysing different PBL magnitudes in order to quantify the differences among the distinct RAMS SM simulations. The first variable examined is the latent heat flux. Fig. 10, which presents the evolution of this magnitude for the two simulated periods. In both cases, we can see that the latent heat flux rises when increasing the initial SM content. Although the SM20 presents values of latent heat around 20-30 W/m^2 in general, SM40 reproduces values between 300 and 400 W/m^2. Comparing SM40 with SM38, differences higher than 100 W/m^2 are obtained in pre-coastal locations. However, these differences are reduced to half for inland station, located in more complex terrain (Fig. 10g,h). The results obtained for individual stations are also illustrated in Fig. 11 for domain D3. This figure shows the distribution of the differences in the latent heat flux between each sensitivity test and the control run. In all cases, a negative bias is obtained for the distinct sensitivity tests. However, a remarkable contrast is observed among the different RAMS runs. For example, differences in the latent heat flux lower than 60 W/m^2 between SM30 and SM20 (Fig. 11a) reach values higher than 300 W/m^2 when subtracting SM40 from SM20. In this regard, Fig. 11 emphasizes how raising the initial SM content is translated into an increase in the latent heat flux within the whole region. Besides this, a descending trend in the latent heat flux was obtained in the second day of simulation, where the deviation from the values observed within the first day suffered a decrease of about 100 W/m^2, with a smaller difference inland (Fig. 10h,j). In general, a specific distribution of the latent heat flux is reproduced by RAMS. However, this magnitude presented a wide spread on the 12 August 2011 (Fig. 10j), where precipitation took place in the Teruel Province (not shown). In this case, we see that the latent heat flux rises in the first half

of the day, reaching values higher than 400 W/m^2 at noon, with a significant difference (about 200 W/m^2) between SM40 and SM38. From this time on, SM40 reproduces low values of the latent heat flux, while drier SM simulation (SM20 and SM30) reproduces a sharp distribution of this magnitude. This behaviour of the model was already observed within the second half of the 11 August 2011 (Fig. 10j), but not to the same extent as on the 12 August 2011. This reduction of the latent heat flux simulated by SM40 in VQM station is associated with a greater cloudiness in the area where this station is located compared to the one reproduced by the other SM contents (Fig. 4). This contrasting result can be seen in Fig. 10j with Fig. 2j. In this regard, condensation occurs in the model in the second half of the day both on 11 and the 12 August 2011. At VQM station, the model produces approximately 2.6 mm of precipitation on the 11 August 2011. In this case, the shortwave radiation observations (Fig. 2j) and satellite observations (Fig. 4) indicate the formation and development of cloudiness over this area. However, although the model using high SM values, specifically SM38 and SM40, produced a slight precipitation within the central part of this day, no precipitation was observed. However, on the 12 August 2011, precipitation is observed and forecasted. In this case, the model starts precipitation before the observations and with a significant initial discharge using SM40. In fact, the model remains closer to the observations drying the soil (not shown). Fig. 10b,d also shows this behaviour with a sharp decrease of the latent heat flux at about 15 UTC and ahead.

The sensible heat flux is included in Fig. 12. In general, values between 300 and 400 W/m^2 are reproduced by the model at noon for the SM38 and SM40 simulations, while values between 500 and 600 W/m^2 are reproduced for the simulations with the lowest initial SM content. Specifically, the differences between SM20 and SM40, reach values up to 200 W/m^2 in the coast and pre-coastal sites. The difference between the two

SM extremes is significantly reduced inland. In order to support these results found at individual stations, maps for the differences in the sensible heat flux between each sensitivity test and the control run within domain D3 are included in Fig. 13. In contrast to the negative bias obtained for these differences in the simulated latent heat flux, the opposite trend is obtained for the distinct sensitivity tests in connection with the sensible heat flux. However, once again a remarkable contrast is observed among the different RAMS runs. In this case, differences in the sensible heat flux higher than 60 W/m^2 between SM30 and SM20 (Fig. 13a) reach values higher than 300 W/m^2 when subtracting SM40 from SM20, especially considering coastal and pre-coastal locations. Besides this, these divergences are reduced in the second day of simulation in comparison with those obtained within the first day. The instability observed inland in the August period may be seen in Fig. 12j, as well as specifically considering the second day of simulation. This figure reflects clearly the differences in the magnitude of the sensible heat flux among stations located in distinct orographic features. In addition, it represents the divergences under different stability conditions. Fig. 12 shows that the maximum of sensible heat flux is delayed when moistening the soil. Comparing this maximum with the daily maximum temperature (Fig. 3), it is observed that the last one is also delayed for the highest SM values compared to the lowest SM contents. This result is the reflection of the usage of the daytime available energy for latent heat flux that eventually reduces sensible heat flux from the surface to the atmosphere (Husain et al., 2014).

On the other hand, increasing the initial SM content in the simulation, produces a decrease of the longwave upward radiation. Differences of the order of 25-50 W/m^2 are observed in general between SM20 and SM40 (not shown). The values in this magnitude produced by the model have their correlation with the 2-m temperature

included in Fig. 3. The daily maximum longwave upward radiation is delayed for about one hour for the highest SM value in relation to the lowest SM content. A slight delay in this magnitude is observed in between. This outcome produces, as mentioned in the previous section, a delay in the diurnal heating and, as a result, the maximum temperature is reached later (Fig. 3). Thus, the lowest SM contents produce warmer and dryer environments, as shown in Figs. 10 and 11, while the highest ones simulate colder and wetter environments.

We would also like to investigate the influence of varying the SM content on the behaviour of the mixing layer height. In order to fulfil this purpose, the potential temperature and the water vapor mixing ratio (Fig. 12) are included in this section for the different weather stations and at 15 UTC corresponding to the first day of simulation. In general, the mixing layer height and the boundary layer structure are rather similar for the two selected periods. In this regard, boundary layer structures are well defined within a height of approximately 500 m over flatter terrain (Fig. 12a,b). Over these areas, even though differences appear among the distinct SM initializations in terms of both the temperature and the humidity fields, little deviation is obtained in the mixing layer height among these RAMS simulations. However, the influence of the mountainous emplacements is well reflected in Fig. 12g,h. In this case, a significant difference is observed when comparing the temperature and the humidity fields produced by the distinct initial SM contents. On the one hand, moistening the soil shows an increase of the mixing layer height of about 500 m for the VIL station. This behaviour is obtained from the two selected periods using the two extremes of SM content. On the other hand, in VQM, the effect of moistening the soil is the opposite, with a strong deepening of the mixing layer height using the lowest SM value. In this case, differences of approximately 1,500 m are found. Fig. 12j shows a strong inversion

layer, with a sudden change in the water vapor mixing ratio. Over this area, a high value of the relative humidity field, higher than 95%, is simulated by SM40, lowering the near-surface temperature by more than 10 ºC in relation to the temperature obtained using SM20 (not shown). In addition, the differences found between VIL and VQM in the mixing layer height seem to be associated with the simulated vertical wind speed. Even though both stations are located inland, the vertical wind speed trend over VIL, changes dramatically in more complex terrain (VQM). In this latter case, the lowest SM values produce a vertical development due to the arrival of warmer and drier air to this area (Fig. 12i). Contrary to this, the highest SM values simulate a sinking of air over VQM but not over VIL (not shown). Thus, the development of the sea-breeze shows little differences in flatter terrain, as was also shown in the MUR sounding (Figs. 7 and 8). On the other hand, changing the initial SM content has a significant effect on the development of the sea-breeze inland. In this case, the differences among the SM simulations depend on the location of the station.

4. Conclusions

This paper evaluates the response and impact of the RAMS-forecasts to modified SM conditions under typical summer mesoscale circulations over Eastern Spain. Two different conditions have been selected, one at the beginning of the summer season (25-26 June 2011) and the other one further into the season (11-12 August 2011). A suite of experiments for both atmospheric conditions have been designed, consisting of five single simulations in which the original low SM content is progressively increased until double its value. In this regard, five different SM values have been used: 0.20, 0.30, 0.35, 0.38 and 0.40 m^3m^{-3}. The lowest SM content is the one originally used within the operational weather forecasting system implemented over this region, based on this mesoscale model. Previous results obtained using this system for the whole 2011

summer season (June-August) led to a difficulty in forecasting the night time near-surface relative humidity, with a tendency to significantly underestimate it, and a relevant overestimation of the daytime 2-m temperature. In this regard, the global bias score of 0.3 ºC obtained at night time rises to 3 ºC during the day (Gómez et al., 2014; Gómez et al., 2015).

The main aim of this study is focused on trying to improve the original results based on the SM initialization. The results show that moistening the soil has a remarkable and positive impact on the simulation of the observed temperature and humidity. In terms of temperature, moistening the soil reduces the daytime bias notably, while still maintaining a low bias at night. Therefore, the forecast of maximum temperatures has been significantly improved while the skilful results already obtained in previous works for the minimum temperatures remain nearly unchanged. In this regard, it has been observed that increase SM results in increase latent heat flux and decrease sensible heat flux, while decrease SM results in decrease latent heat flux and increase sensible heat flux.

Additionally, it seems that RAMS is more sensitive to moistening the soil than to drying it. In this regard, model simulations show that a slight difference at high SM content produces more differences among them than a larger modification of the SM at lower values. Furthermore, applying the lowest SM contents, a greater bias in the moisture field is observed as the simulations progresses in comparison with that obtained on the first day of simulation. This result is not that clear in the highest SM contents.

Although a concrete SM value has not been detected to better fit the observations, it has been found that it is essential in general to increase the initial SM content in order to reproduce the observations. Still, some locations fit the

measurements in a better way by using the lowest SM value, as is the case of XAT weather station (Fig. 1). It must be remembered here that a homogeneous initialization has been used in the current study. Therefore, the results obtained indicate that a heterogeneous SM initialization could probably produce a better tuning of the model in relation to the observations. Thus, additional studies on this issue should be performed in the future to assess the model sensitivity to heterogeneous information. In this regard, the use of remote sensing products, particularly those retrieved from the Soil Moisture and Ocean Salinity (SMOS) satellite, will be used in order to evaluate the potential usefulness of this data for RAMS initialization and assimilation.

On the other hand, in those areas where a well established mesoscale circulation is observed, the results obtained for the two selected periods are rather alike. Consequently, it seems that systematic errors are found and also improved on, depending on the initial SM content for the simulation of these sort of atmospheric conditions.

In summary, the current study highlights that a simulated colder and wetter environment is needed in order to faithfully reproduce the measured 2-m temperature and the near-surface relative humidity daily cycles. This can be achieved varying the initial SM content. Consequently, moistening the soil not only improves, in general, the modelling of these magnitudes on the surface but also in upper levels. However, the improvement detected for the thermodynamic variables is not reflected in the wind speed over flatter terrain. In this regard, modifying the SM has little effect on the model output, thus supporting the overestimation already found for this magnitude using the original SM content (0.20 m^3m^{-3}). Therefore, additional studies should be performed with the aim of trying to simulate wind speed closer to the observations under the corresponding atmospheric and geographical conditions covered in this work.

Acknowledgement

This work has been funded by the Regional Government of Valencia through the project PROMETEOII/2014/086. NCEP is acknowledged for providing the FNL analysis data for RAMS initialization. Environmental Prediction/National Weather Service/NOAA/U.S National Centres. Department of Commerce (2000): NCEP FNL Operational Model Global Tropospheric. Analyses, continuing from July 1999. Research Data Archive from 'The National Centre for Atmospheric Research', Computational and Information Systems Laboratory. Dataset. http://rda.ucar.edu/datasets/ds083.2(accessed 25 August 2014.) The authors acknowledge the Atmospheric Soundings portal of the University of Wyoming (http://weather.uwyo.edu/upperair/sounding.html) for providing the radiosonde data. We would like to thank the Spanish Ministry of Agriculture, Food and Environment for making the surface observations available through the SIAR system. Finally, we also thank the two anonymous reviewers for their constructive comments and suggestions, which have greatly improved this paper.

References

Azorin-Molina C, Chen D (2009). A climatological study of the influence of synoptic-scale flows on sea breeze evolution in the Bay of Alicante (Spain). Theoretical and Applied Climatology 96: 249–260. doi: 10.1007/s00704-008-0028-2.

Azorin-Molina C, Chen D, Tijm S, Baldi M (2011). A multi-year study of sea breezes in a Mediterranean coastal site: Alicante (Spain). International Journal of Climatology 31: 468–486. doi:10.1002/joc.2064.

Azorin-Molina C, Tijm S, Ebert EE, Vicente-Serrano SM, Estrela MJ (2014). Sea breeze thunderstorms in the eastern Iberian Peninsula. Neighborhood verification of HIRLAM and HARMONIE precipitation forecasts. Atmospheric Research 139: 101-155. doi: 10.1016/j.atmosres.2014.01.010.

Brisson A, Le Borgne P, Marsouin A (1999). Development of Algorithms for Surface Solar Irradiance retrieval at O&SI SAF low and Mid Latitude, Météo-France/CMS, Lannion.

Chen, C, Cotton, WR (1983). A one-dimensional simulation of the stratocumulus-capped mixed layer. Boundary-Layer Meteorology 25: 289–321.

Cotton WR, Pielke RAS, Walko RL, Liston GE, Tremback CJ, Jiang H, McAnelly RL, Harrington JY, Nicholls ME, Carrio GG, McFadden JP (2003). RAMS 2001: Current status and future directions. Meteorology and Atmospheric Physics 82 (1-4): 5-29.

Geiger B, Meurey C, Lajas D, Franchisteguy L, Carrer D, Roujean, J-L (2008). Near real-time provision of downwelling shortwave radiation estimates derived from satellite observations, Meteorological Applications, 15: 411–420. doi:10.1002/met.84.

Gómez I, Estrela MJ (2010). Design and development of a java-based graphical user interface to monitor/control a meteorological real-time forecasting system. Computers & Geosciences 36: 1345-1354. doi:10.1016/j.cageo.2010.05.005.

Gómez I, Caselles V, Estrela, MJ, Niclòs R (2014). RAMS-forecasts comparison of typical summer atmospheric conditions over the Western Mediterranean coast. Atmospheric Research, 145-146: 130-151. doi: 10.1016/j.atmosres.2014.03.018.

Gómez I, Estrela, MJ, Caselles, V (2015). Verification of the RAMS-based operational weather forecast system in the Valencia Region: a seasonal comparison. Natural Hazards, 75: 1941–1958. doi: 10.1007/s11069-014-1408-9.

Husain SZ, Bélair S, Leroyer S (2014). Influence of Soil Moisture on Urban Microclimate and Surface-Layer Meteorology in Oklahoma City. Journal of Applied Meteorology and Climatology, 53: 83–98.

Kala J, Lyons TJ, Abbs DJ, Nair US (2010). Numerical Simulations of the Impacts of Land-Cover Change on a Southern Sea Breeze in South-West Western Australia. Boundary-Layer Meteorology, 135: 485-503. doi: 10.1007/s10546-010-9486-z.

LSA SAF (2015). The EUMETSAT Satellite Application Facility on Land Surface Analysis (LSA SAF), Product User Manual, Down-welling Shortwave Flux (DSSF), available at: https://landsaf.meteo.pt/algorithms.jsp?seltab=1\&starttab=1. Accessed 5 March 2015.

Ma Y, Lyons TJ (2000) Numerical simulation of a sea-breeze under dominant synoptic conditions at Perth. Meteorology and Atmospheric Physics, 73: 89-10.

Mellor G, Yamada T (1982). Development of a turbulence closure model for geophysical fluid problems. Reviews of Geophysics and Space Physics 20: 851-875.

Miao JF, Kroon LJM, Vilà-Guerau de Arellano J, Holtslag AAM (2003). Impacts of topography and land degradation on the sea breeze over eastern Spain. Meteorolology and Atmospheric Physics, 84: 157–170.

Millán, MM, Salvador, R, Mantilla, E, Kallos G (1997). Photooxidants dynamics in the Mediterranean basin in summer: Results from European research projects. Journal of Geophysical Research, 102(D7): 8811–8823.

Millán MM, Mantilla E, Salvador R, Carratalá A, Sanz MJ, Alonso L, Gangoiti G, Navazo M (2000). Ozone cycles in the Western Mediterranean basin: Interpretation of monitoring data in complex coastal terrain. Journal of Applied Meteorology, 39 (4): 487–508.

Miró J, Estrela MJ, Pastor F, Millán M (2009). Análisis comparativo de tendencias en la precipitación, por distintos inputs, entre los dominios hidrológicos del Segura y del Júcar (1958-2008), in Spanish. Investigaciones Geográficas, 49: 129-157.

Molinari J (1985). A general form of kuo's cumulus parameterization. Monthly Weather Review, 113: 1411-1416.

NCEP (2014). National Centers for Environmental Prediction/National Weather Service/NOAA/U.S. Department of Commerce (2000): NCEP FNL Operational Model Global Tropospheric Analyses, continuing from July 1999. Research Data Archive at the National Center for Atmospheric Research, Computational and Information Systems Laboratory. Dataset. http://rda.ucar.edu/datasets/ds083.2. Accessed 25 August 2014.

Pérez-Landa G, Ciais P, Sanz MJ, Gioli B, Miglietta F, Palau JL, Gangoiti G, Millán M (2007). Mesoscale circulations over complex terrain in the Valencia coastal region, Spain. Part 1: Simulation of diurnal circulation regimes. Atmospheric Chemistry and Physics, 7: 1835-1849.

Physick WL (1980). Numerical experiments on the inland penetration of the sea breeze. Quarterly Journal of the Royal Meteorological Society, 106: 735-746.

Pielke Sr. RA (2013). Mesoscale meteorological modeling. 3rd Edition. Academic Press, San Diego, CA, 760 pp.

Quintanar AI, Mahmood R, Loughrin J, Lovanh NC (2008). A coupled MM5-NOAH land surface model-based assessment of sensitivity of planetary boundary layer variables to anomalous soil moisture conditions. Physical Geography, 29: 54-78.

Suarez A, Mahmood R, Quintanar AI, Beltrán-Przekurat A, Pielke R (2014). A comparison of the MM5 and the Regional Atmospheric Modeling System simulations for land-atmosphere interactions under varying soil moisture. Tellus A, 66: 1-17.

Walko RL, Cotton WR, Meyers MP, Harrington JY (1995). New RAMS cloud microphysics parameterization. Part I: The single-moment scheme. Atmospheric Research, 38: 29-62.

Walko RL, Band LE, Baron J, Kittel TGF, Lammers R, Lee TJ, Ojima D, Pielke RA, Taylor C, Tague C, Tremback CJ, Vidale PL (2000). Coupled atmospheric-biophysics-hydrology models for environmental modeling. Journal of Applied Meteorology, 39: 931-944.

Yan H, Anthes RA (1988). The effect of variations in surface moisture on mesoscale circulations. Monthly Weather Review, 116: 192-208.

Figure captions

Fig. 1. Simulation domain specification and orography (m) of the RAMS model on domain D1 in addition to the weather station sites and orography for the finer domain (D3).

Fig. 2. Time series of observed (triangle) and simulated (solid lines) incident surface flux of shortwave radiation (W/m^2), for different surface weather stations during the June period (left): SAN (a), SEG (c), XAT (e), VIL (g), VQM (i), and the August period (right): SAN (b), SEG (d), XAT (f), VIL (h), VQM (j).

Fig. 3. Same as Fig. 2, but for the 2-m temperature (^oC).

Fig. 4. Comparison of the incident surface shortwave radiation flux (W/m^2) over domain D3 on 12 August 2011 at 15 UTC: SM20 (a), SM30 (b), SM35 (c), SM38 (d), SM40 (e), down-welling surface shortwave radiation flux (DSSF), obtained by means of the SEVIRI sensor (f).

Fig. 5. Same as Fig. 2, except for the near-surface relative humidity (%).

Fig. 6. Same as Fig. 2, except for the 10-m wind speed (m/s).

Fig. 7. Same as Fig. 2, except for the 10-m u-component and the 10-m v-component of the wind (m/s).

Fig. 8. Observed (triangle) and simulated (solid lines) vertical profiles for the MUR sounding station and for the June period. 25 June at 12 UTC (left): potential temperature, (K; a), relative humidity (%; c), wind speed (m/s; e) and wind direction (^{o}; g). 26 June at 00 UTC (right): potential temperature, (K; b), relative humidity (%; d), wind speed (m/s; f) and wind direction (^{o}; h).

Fig. 9. Same as Fig. 7, but for the August period: 11 August at 00 UTC (left) and 11 August at 12 UTC (right).

Fig. 10. Comparison of simulated latent heat flux (W/m^2), for different surface weather stations during the June period (left): SAN (a), SEG (c), XAT (e), VIL (g), VQM (i), and the August period (right): SAN (b), SEG (d), XAT (f), VIL (h), VQM (j).

Fig. 11. Comparison of the latent heat flux (W/m^2) spatial distribution over domain D3 on 25 June 2011 at 12 UTC: SM20-SM30 (a), SM20-SM35 (b), SM20-SM38 (c), SM20-SM40 (d).

Fig. 12. Same as Fig. 10, but for the sensible heat flux (W/m^2).

Fig. 13. Same as Fig. 11, but for the sensible heat flux (W/m^2).

Fig. 14. Comparison of simulated water vapor mixing ratio (g/Kg; left) and potential temperature (C; right) vertical profiles, 25 June 2011 at 15 UTC (left): SAN (a), SEG (c), XAT (e), VIL (g), VQM (i), and 11 August 2011 at 15 UTC: SAN (b), SEG (d), XAT (f), VIL (h), VQM (j).

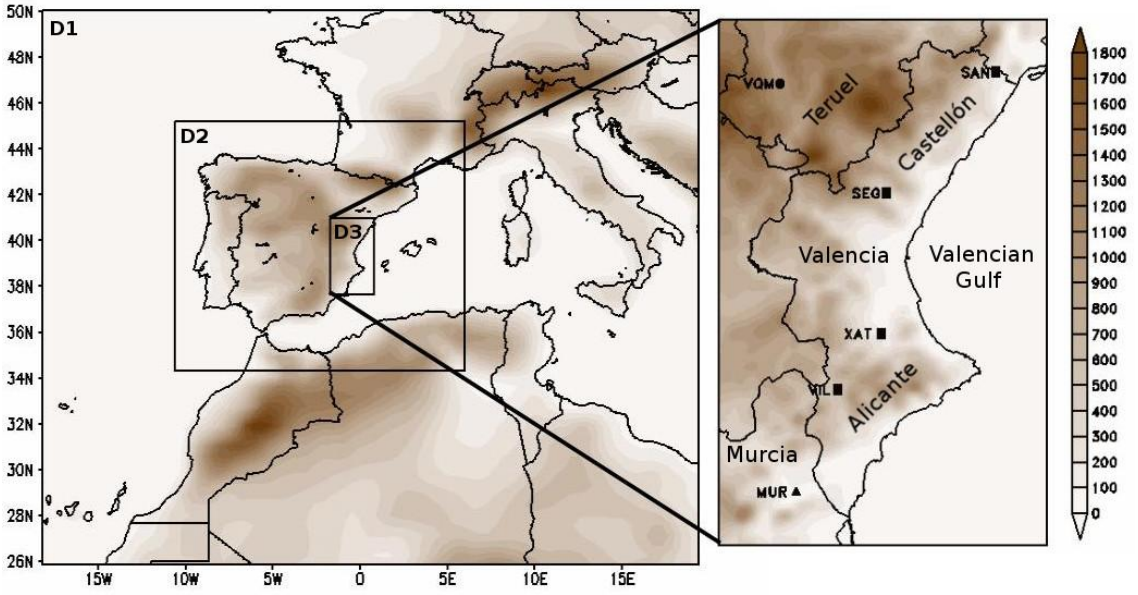
D1
D2
D3
50N
48N
46N
44N
42N
40N
38N
36N
34N
32N
30N
28N
26N
15W
10W
5W
0
5E
10E
15E
VQM
Teruel
SAN
Castellón
SEG
Valencia
Valencian
Gulf
XAT
VIL
Alicante
Murcia
MUR
1800
1700
1600
1500
1400
1300
1200
1100
1000
900
800
700
600
500
400
300
200
100
0

Figure 1

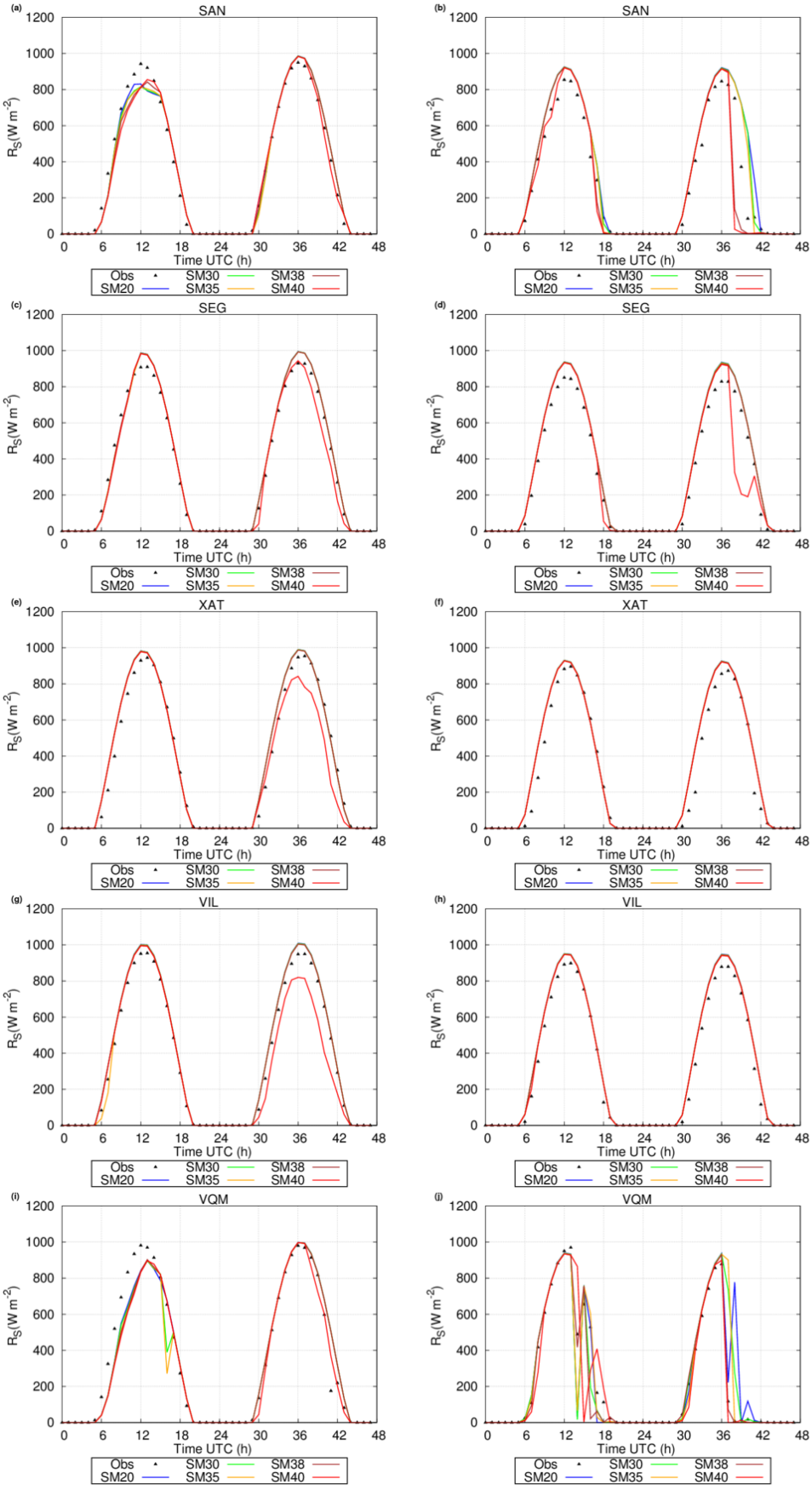
(a)
SAN
(b)
SAN
(c)
SEG
(d)
SEG
(e)
XAT
(f)
XAT
(g)
VIL
(h)
VIL
(i)
VQM
(j)
VQM
R_S(W m^{-2})
Time UTC (h)
Obs
SM20
SM30
SM35
SM38
SM40

Figure 2

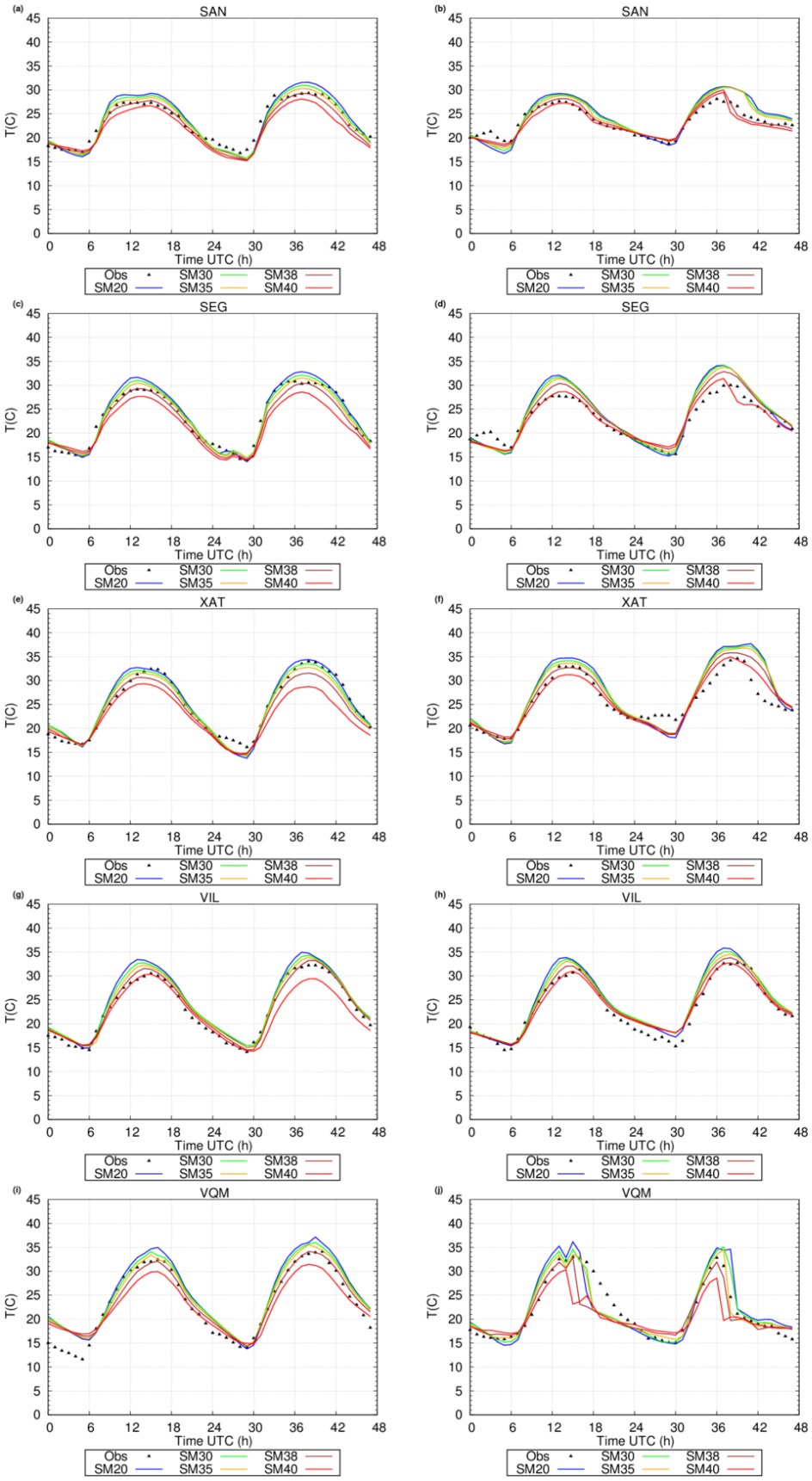
(a)
SAN
(b)
SAN
(c)
SEG
(d)
SEG
(e)
XAT
(f)
XAT
(g)
VIL
(h)
VIL
(i)
VQM
(j)
VQM
T(C)
Time UTC (h)
Obs
SM20
SM30
SM35
SM38
SM40

Figure 3

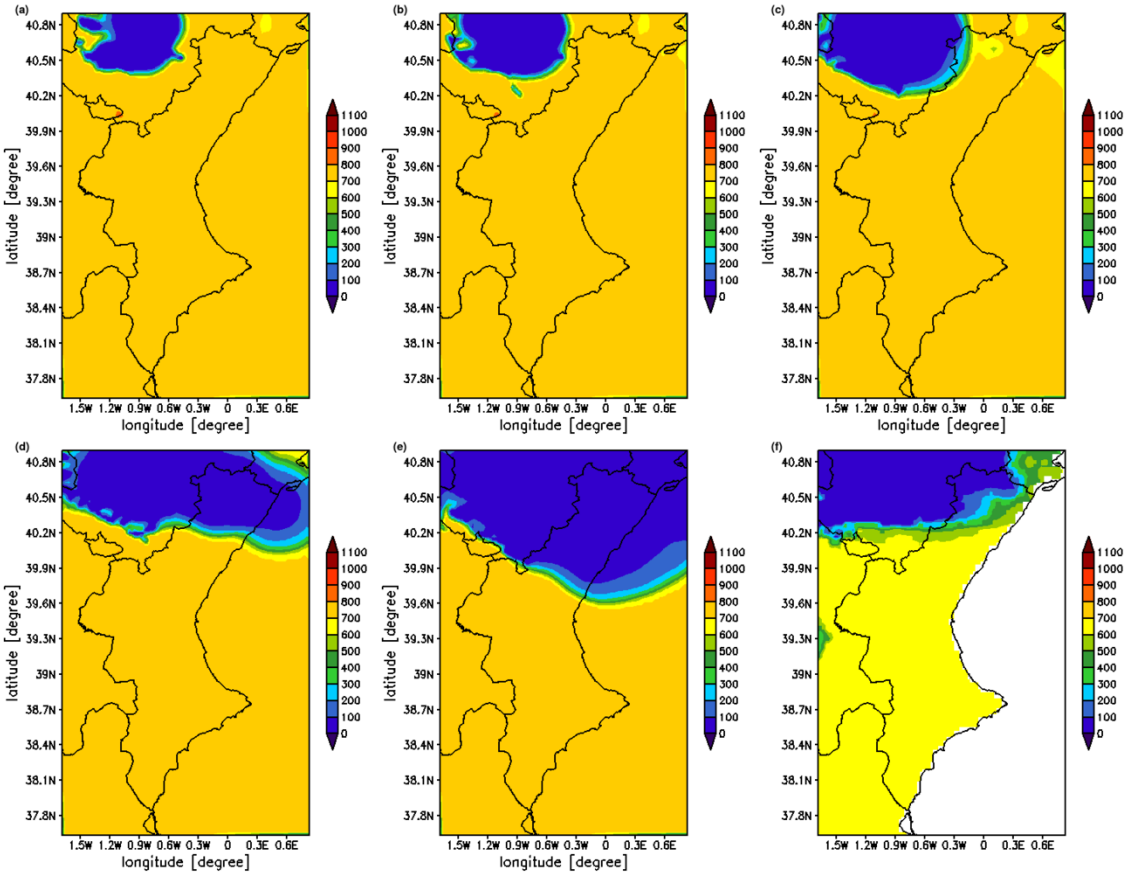
(a)
(b)
(c)
(d)
(e)
(f)
latitude [degree]
longitude [degree]
40.8N
40.5N
40.2N
39.9N
39.6N
39.3N
39N
38.7N
38.4N
38.1N
37.8N
1.5W 1.2W 0.9W 0.6W 0.3W 0 0.3E 0.6E
1100
1000
900
800
700
600
500
400
300
200
100
0

Figure 4

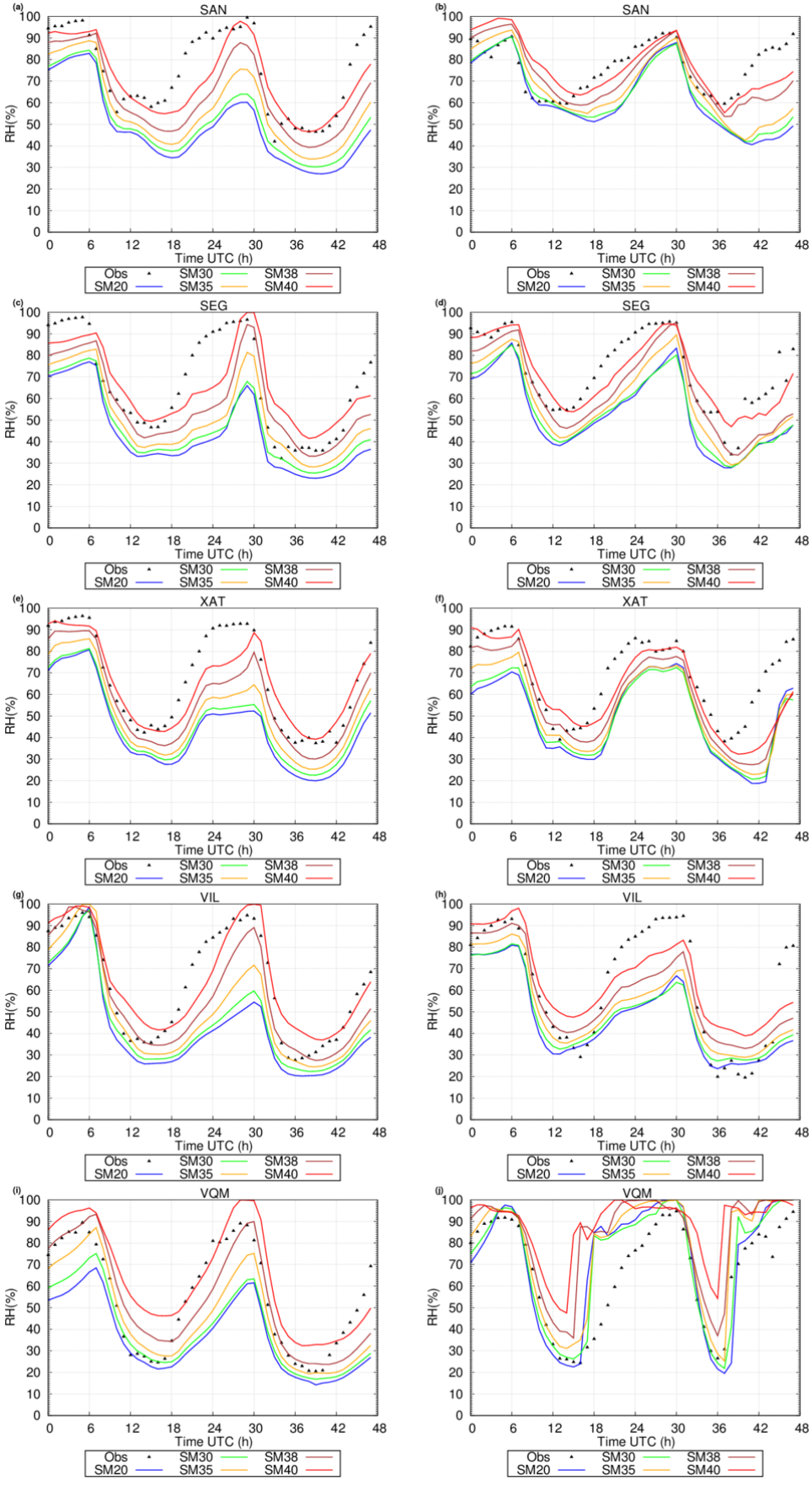
(a)
SAN
(b)
SAN
(c)
SEG
(d)
SEG
(e)
XAT
(f)
XAT
(g)
VIL
(h)
VIL
(i)
VQM
(j)
VQM
RH(%)
Time UTC (h)
Obs
SM20
SM30
SM35
SM38
SM40

Figure 5

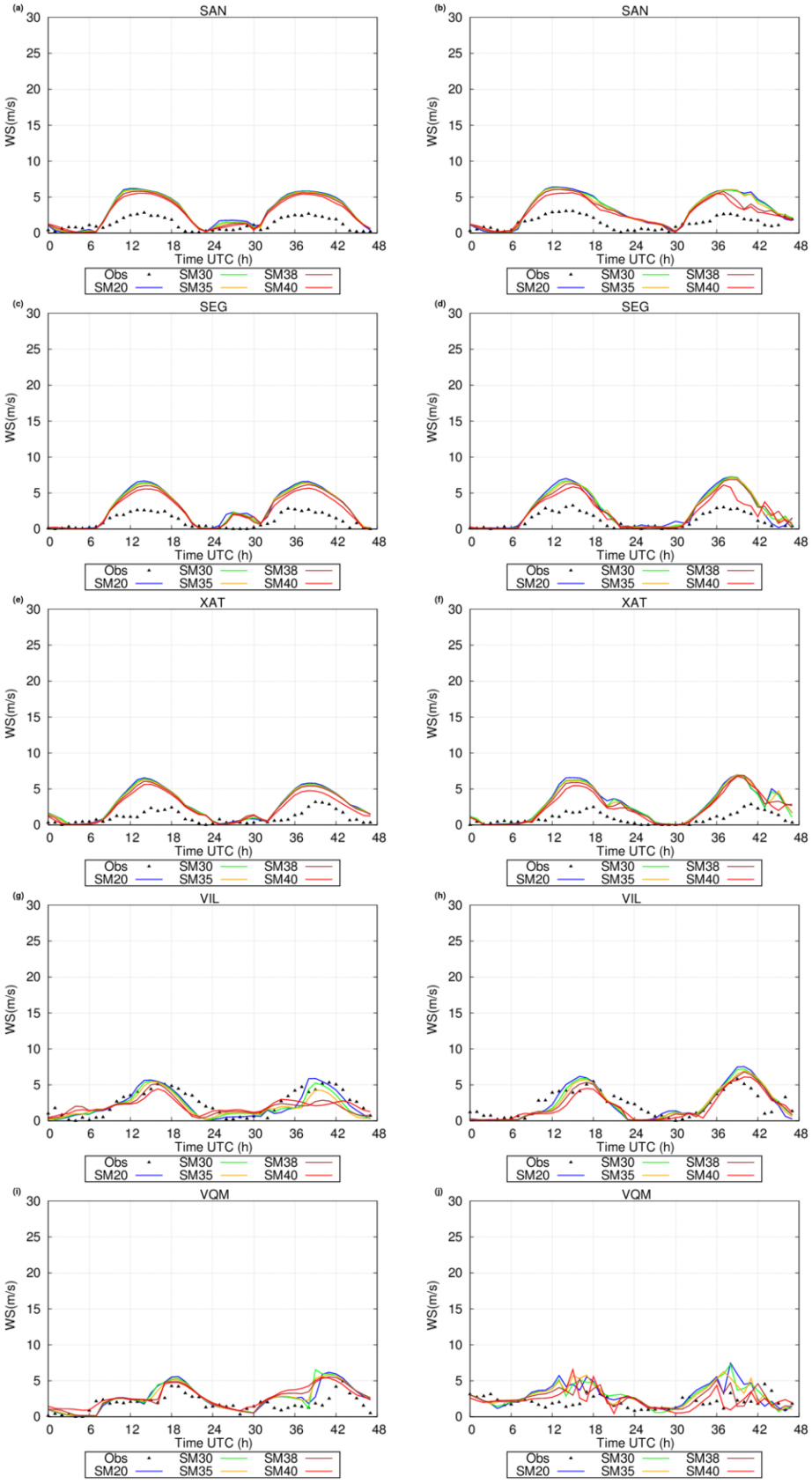
(a)
SAN
(b)
SAN
(c)
SEG
(d)
SEG
(e)
XAT
(f)
XAT
(g)
VIL
(h)
VIL
(i)
VQM
(j)
VQM
WS(m/s)
Time UTC (h)
Obs
SM20
SM30
SM35
SM38
SM40

Figure 6

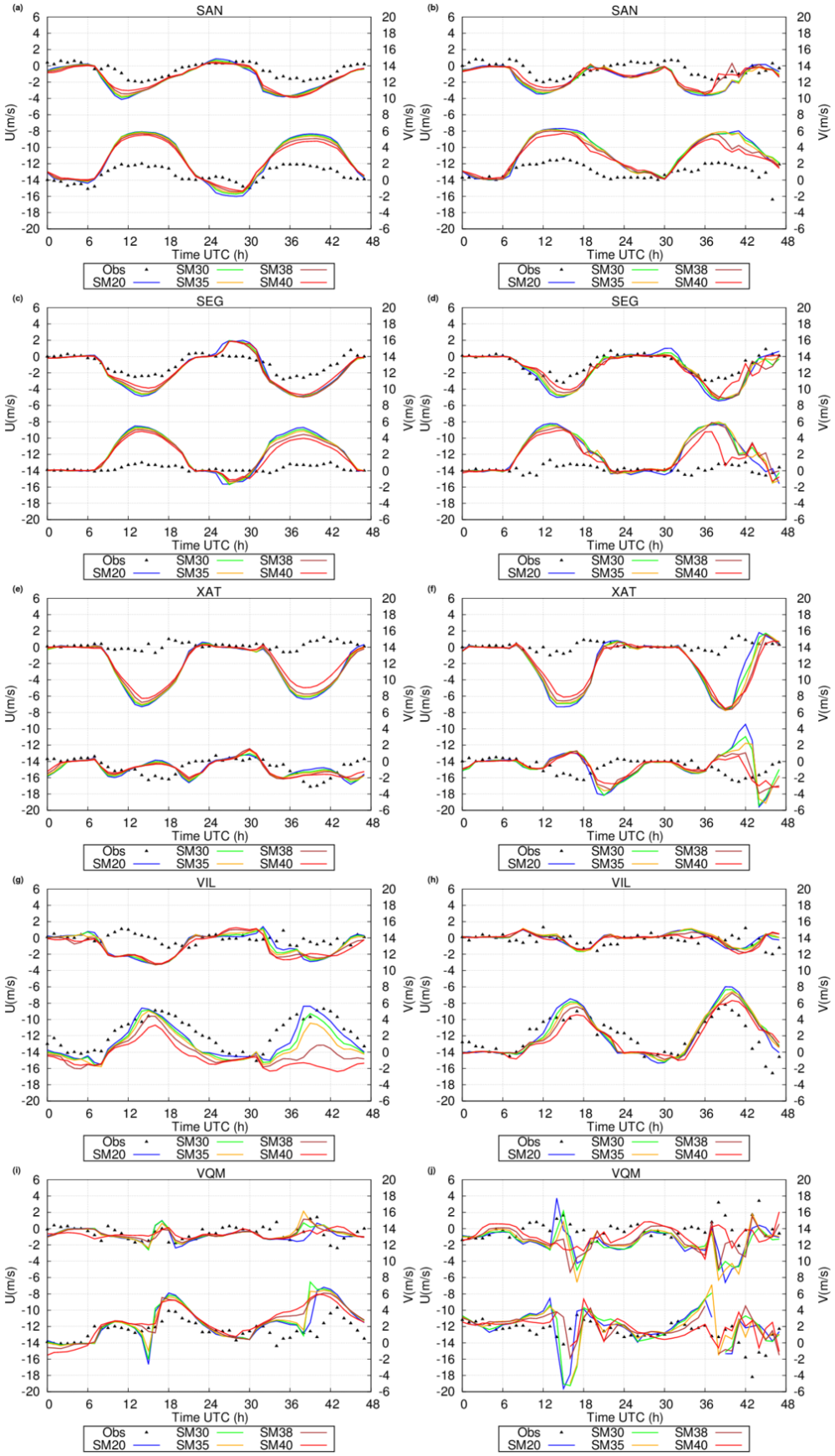
(a)
SAN
(b)
SAN
(c)
SEG
(d)
SEG
(e)
XAT
(f)
XAT
(g)
VIL
(h)
VIL
(i)
VQM
(j)
VQM
U(m/s)
V(m/s)
Time UTC (h)
Obs
SM20
SM30
SM35
SM38
SM40

Figure 7

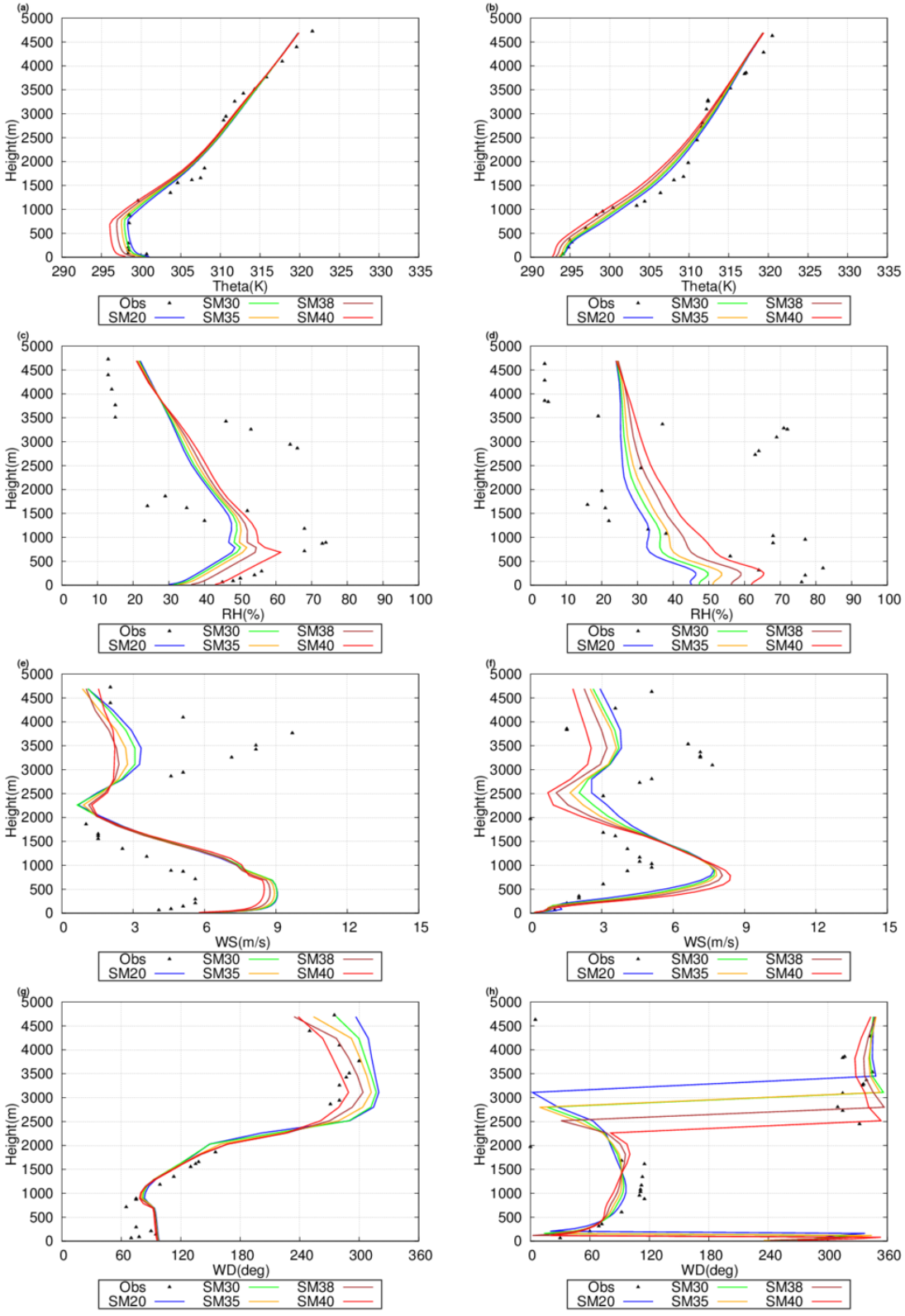
(a)
(b)
(c)
(d)
(e)
(f)
(g)
(h)
Height(m)
Theta(K)
RH(%)
WS(m/s)
WD(deg)
Obs
SM20
SM30
SM35
SM38
SM40

Figure 8

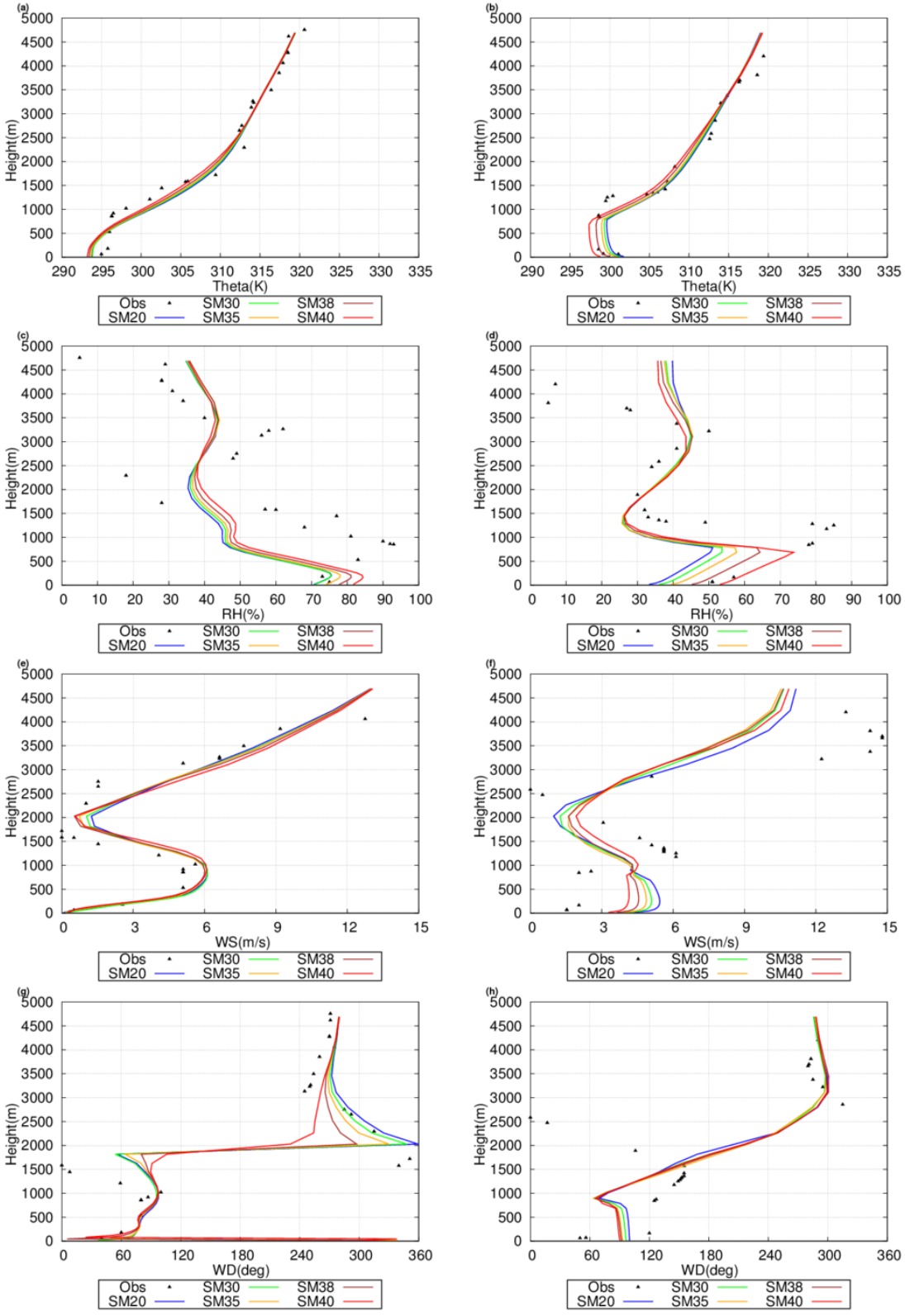
(a)
(b)
(c)
(d)
(e)
(f)
(g)
(h)
Height(m)
Theta(K)
RH(%)
WS(m/s)
WD(deg)
Obs
SM20
SM30
SM35
SM38
SM40

Figure 9

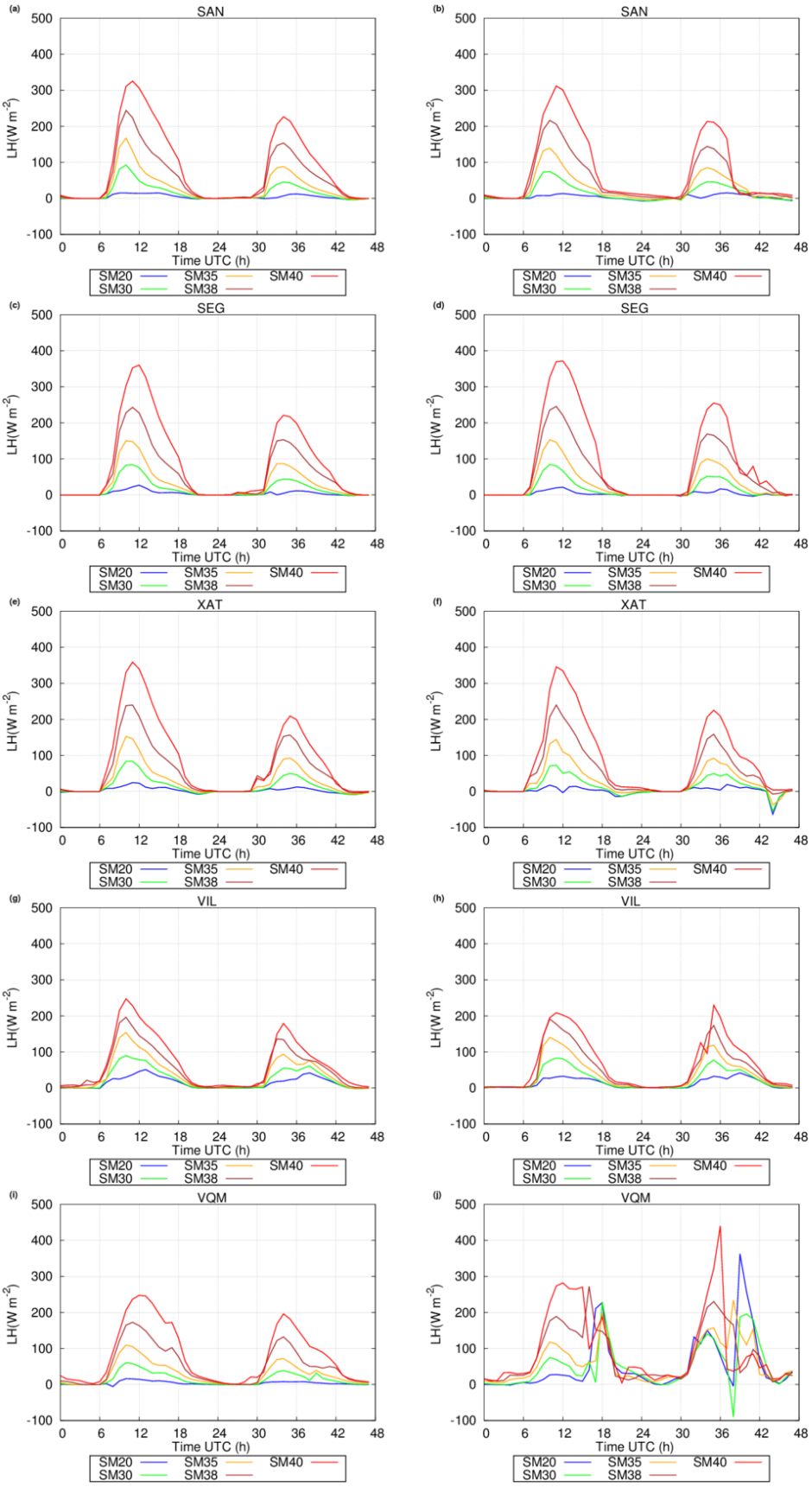
(a)
SAN
(b)
SAN
(c)
SEG
(d)
SEG
(e)
XAT
(f)
XAT
(g)
VIL
(h)
VIL
(i)
VQM
(j)
VQM
LH(W m-2)
Time UTC (h)
SM20
SM35
SM40
SM30
SM38

Figure 10

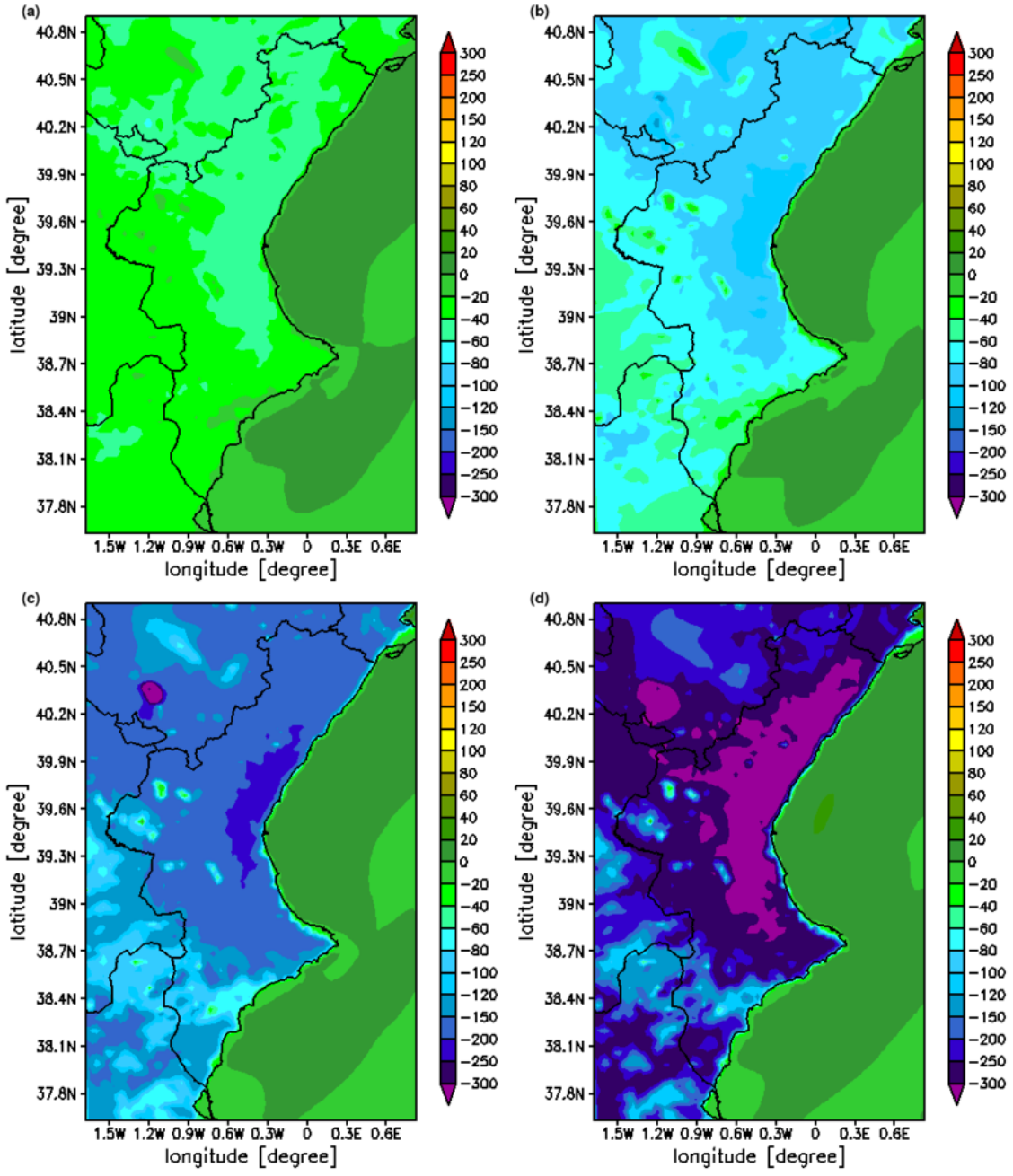
(a)
(b)
(c)
(d)
40.8N
40.5N
40.2N
39.9N
39.6N
39.3N
39N
38.7N
38.4N
38.1N
37.8N
latitude [degree]
1.5W 1.2W 0.9W 0.6W 0.3W 0 0.3E 0.6E
longitude [degree]
300
250
200
150
120
100
80
60
40
20
0
−20
−40
−60
−80
−100
−120
−150
−200
−250
−300

Figure 11

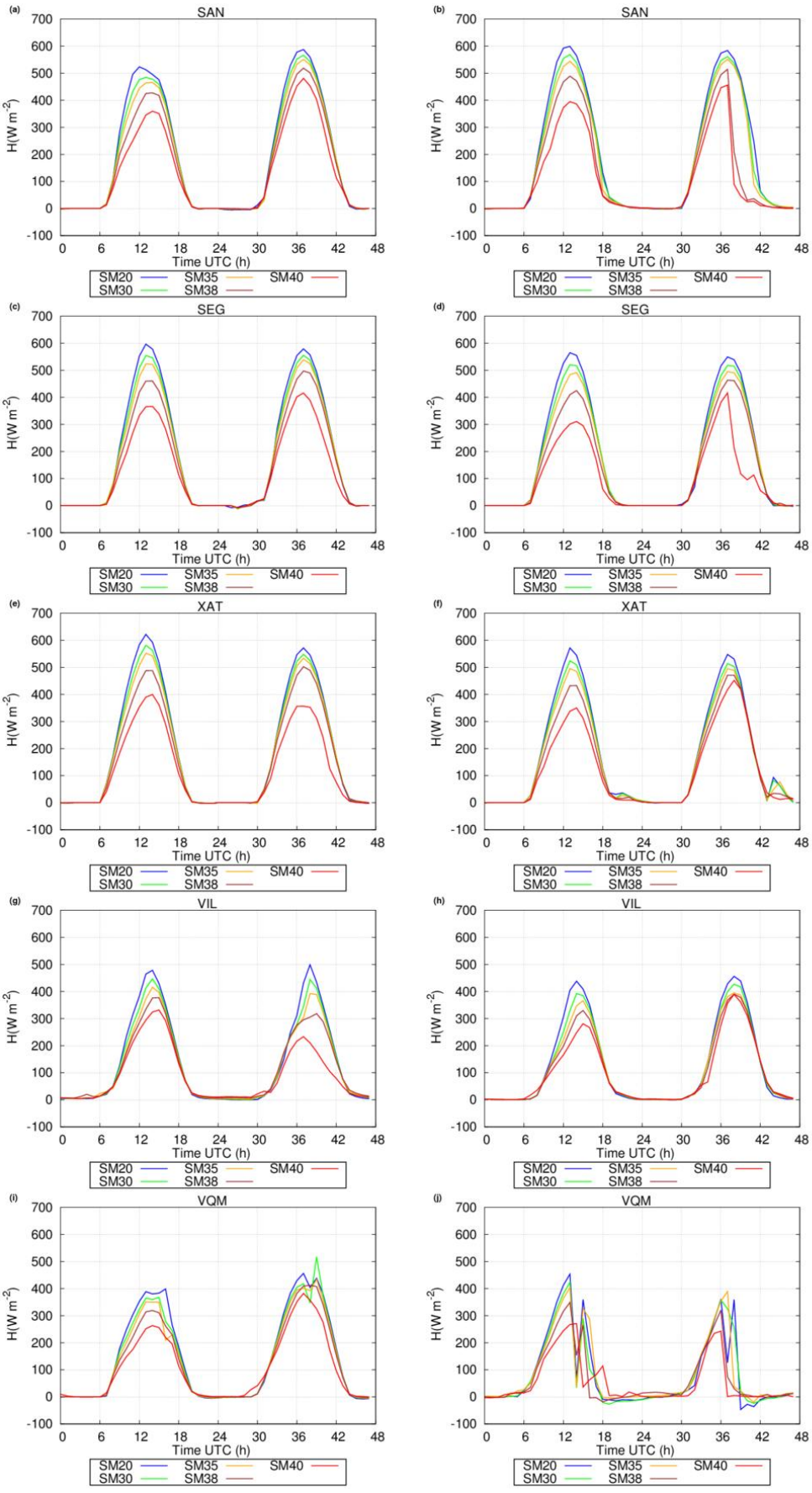
(a)
SAN
(b)
SAN
(c)
SEG
(d)
SEG
(e)
XAT
(f)
XAT
(g)
VIL
(h)
VIL
(i)
VQM
(j)
VQM
H(W m-2)
Time UTC (h)
SM20
SM30
SM35
SM38
SM40

Figure 12

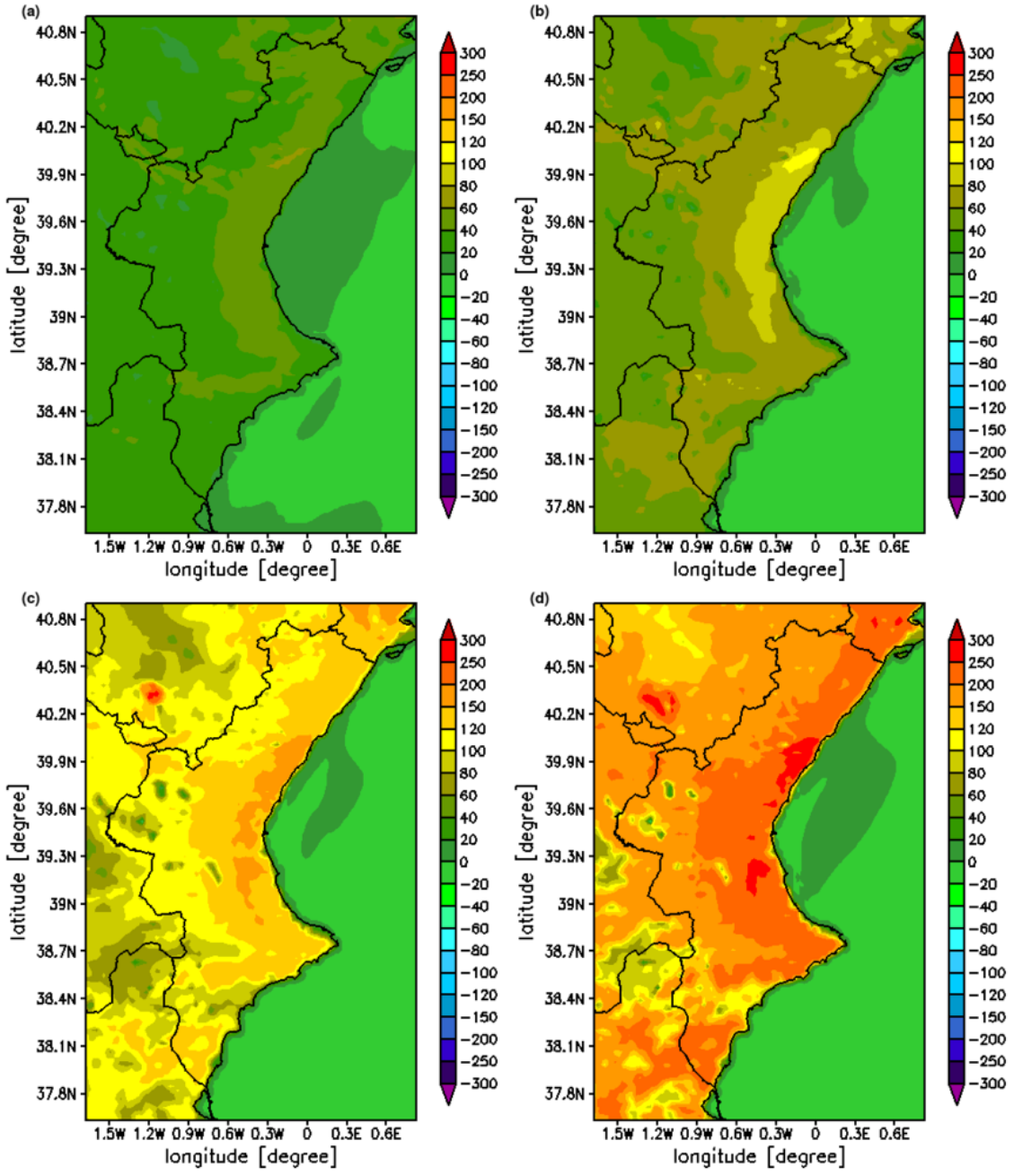
(a)
(b)
(c)
(d)
40.8N
40.5N
40.2N
39.9N
39.6N
39.3N
39N
38.7N
38.4N
38.1N
37.8N
latitude [degree]
1.5W 1.2W 0.9W 0.6W 0.3W 0 0.3E 0.6E
longitude [degree]
300
250
200
150
120
100
80
60
40
20
0
−20
−40
−60
−80
−100
−120
−150
−200
−250
−300

Figure 13

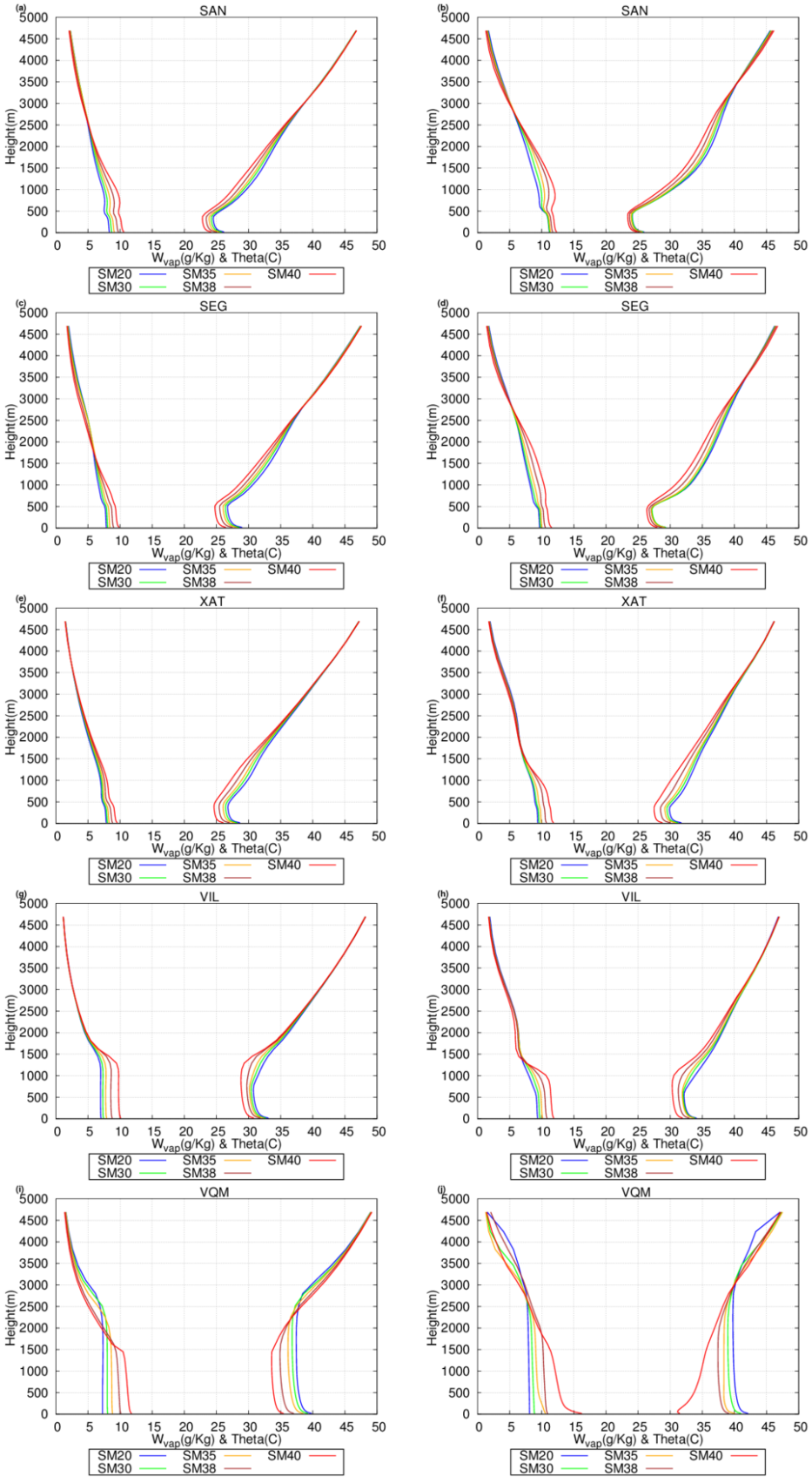
(a)
SAN
(b)
SAN
(c)
SEG
(d)
SEG
(e)
XAT
(f)
XAT
(g)
VIL
(h)
VIL
(i)
VQM
(j)
VQM
Height(m)
W_vap(g/Kg) & Theta(C)
SM20
SM30
SM35
SM38
SM40

Figure 14